

Quantum Rabi dynamics of trapped atoms far in the deep strong coupling regime

Johannes Koch,¹ Geram Hunanyan,¹ Till Ockenfels,¹ Enrique Rico,^{2,3} Enrique Solano^{2,3,4,5} and Martin Weitz¹

¹*Institut für Angewandte Physik, Universität Bonn, Wegelerstr. 8, 53115 Bonn, Germany*

²*Department of Physical Chemistry, University of the Basque Country UPV/EHU, Apartado 644, 48080 Bilbao, Spain*

³*IKERBASQUE, Basque Foundation for Science, Plaza Euskadi 5, 48009 Bilbao, Spain*

⁴*Kipu Quantum, Kurwenalstrasse 1, 80804 Munich, Germany*

⁵*International Center of Quantum Artificial Intelligence for Science and Technology (QuArtist) and Department of Physics, Shanghai University, 200444 Shanghai, China*

The coupling of a two-level system with an electromagnetic field, whose fully quantized field version is known as the quantum Rabi model^{1,2}, is among the central topics of quantum physics and recent quantum information technologies^{3,4,5,6,7,8,9}. When the coupling strength becomes stronger than the decoherence rate the so-called strong coupling regime is reached, with mixed states of the two-level system and the field mode becoming relevant¹⁰. Further, when the coupling strength reaches the field mode frequency the deep strong coupling regime is approached and excitations can be created out of the vacuum^{11,12}, see also recent works with effective spin-field, trapped ion, and superconducting qubit-oscillator implementations^{13,14,15}.

Here we demonstrate a novel approach for the realization of a periodic variant of the quantum Rabi model using two coupled quantized mechanical modes of cold atoms in optical potentials, which has allowed us to reach a Rabi coupling strength of 6.5 times the field mode frequency, i.e., far in the deep strong coupling regime. For the first time, the coupling term dominates over all other energy scales. Field mode creation and annihilation upon e.g., de-excitation of the two-level

system here approach equal magnitudes, and we observe the atomic dynamics in this novel experimental regime, revealing a subcycle timescale raise in bosonic field mode excitations, in good agreement with theoretical predictions. In a measurement recorded in the basis of the coupling term of the quantum Rabi Hamiltonian, the observed dynamics freezes for small frequency splittings of the two-level system, but revives for larger splittings. Our concept demonstrates a route to realize quantum-engineering applications in yet unexplored parameter regimes^{4,16}.

The motivation to develop the quantum Rabi model, which is also termed the single-mode spin-boson model, mostly stems from the quest to obtain a complete quantum description of the interaction of matter and light². Other than the earlier developed Jaynes-Cummings model¹⁷, in addition to the co-rotating, it also includes the counter-rotating terms of the interaction Hamiltonian, which has striking consequences as the coupling strength approaches the eigenfrequency of the oscillator, a regime that is not accessible to natural light-matter interactions. On the theoretical side, an analytic solution of the full quantum Rabi model has more recently been found¹⁸. So far, experimental implementations of the quantum Rabi model, using cold-atom, ion trap, and Josephson qubit systems, have allowed to reach values of the ratio of coupling g and bosonic mode frequency ω of up to $g/\omega \approx 1.34$.¹⁵

Using a novel experimental approach based on the coupling of an effectively spin-like and a bosonic vibrational mode respectively, we demonstrate a coupling ratio of $g/\omega \approx 6.5$, achieving clear domination of the coupling strength over all other energy scales for the first time. Our experimental approach uses a two-level system provided by two Bloch bands in an optical lattice and a bosonic mode provided by the quantized atomic vibration in a superimposed optical dipole trap potential. For short interaction times, predictions of the quantum Rabi model in the investigated extreme

parameter regime are experimentally validated, and for long interaction times we observe the onset of the dynamics of a proposed generalized periodic version of this model¹⁹.

A schematic of the relevant vibrational modes of ultracold atoms in the implemented potential landscape is shown in Fig. 1a, see the left hand side for an illustration of the bosonic mode represented by the quantized atomic vibration in the harmonic trapping potential. The right hand side shows the superimposed periodic lattice potential serving to implement the two-state system in its Bloch band structure. Before discussing the degree of coupling between these two quantized modes for typical experimental parameters, we briefly describe our experimental implementation, see Fig. 1b for a schematic of the used setup. A harmonic trapping potential for a cold cloud of rubidium atoms (⁸⁷Rb) is generated by a focused laser beam derived from a CO₂-laser operating near a wavelength of 10.6 μm, which due to its large detuning from the atomic resonances allows for the creation of deep potentials while keeping the scattering rate low enough to prevent spurious heating of the atomic ensemble. The additional lattice potential, of spatial periodicity $\frac{\lambda}{4}$, where $\lambda = 783.5$ nm denotes the wavelength of the driving laser beams, is generated by the dispersion of Doppler-sensitive Raman transitions^{20,21}, see Fig. 1c for the used level scheme. These effective four-photon processes couple atoms in momentum states $| - 2\hbar k + q \rangle$ and $| 2\hbar k + q \rangle$, where q denotes the atomic quasimomentum and $k = \frac{2\pi}{\lambda}$. The coupling leads to a splitting between bands, see Fig. 1d for the resulting atomic dispersion, and we in the following restrict the discussion to the lowest two bands. At the band crossing (at $q = 0$) we are left with the eigenstates of the two-level system of the quantum Rabi Hamiltonian, with $|g\rangle = \frac{1}{\sqrt{2}}(| - 2\hbar k \rangle + | 2\hbar k \rangle)$ and $|e\rangle = \frac{1}{\sqrt{2}}(| - 2\hbar k \rangle - | 2\hbar k \rangle)$ respectively, whose coupling to the bosonic mode provided by the vibrational dynamics we are interested in. It can be shown that the atomic dynamics is described by the Hamiltonian (see Methods and Ref. 19):

$$\hat{H} = \hbar\omega \hat{a}^\dagger \hat{a} + \frac{\hbar\omega_q}{2} \sigma_z + i\hbar g \sigma_x (\hat{a}^\dagger - \hat{a}) \quad (1)$$

where \hat{a}^\dagger and \hat{a} correspond to creation and annihilation operators of the bosonic field, with as usual

$\hat{x} = \sqrt{\frac{\hbar}{2m\omega}} (\hat{a} + \hat{a}^\dagger)$, $\hat{q} = \sqrt{-\frac{\hbar m \omega}{2}} (\hat{a}^\dagger - \hat{a})$, and σ_x and σ_z are Pauli matrices that act on two-component spinors with the components describing coarse-grain atomic wavefunctions in upper and lower bands respectively. Further, $\hbar\omega_q$ is the energetic spacing between the bands at the position of the crossing (Fig. 1d), which can be adjusted by the depth of the lattice potential, and $g = k \sqrt{\frac{2\hbar\omega}{m}}$ is the coupling constant. Typical experimental parameters are a trap oscillation frequency $\frac{\omega}{2\pi} \in [350, 750]$ Hz, for which we arrive at $\frac{g}{2\pi}$ between 2290 Hz and 3090 Hz, so that the deep strong coupling limit is well fulfilled, meaning that the two motional modes present in the system, see also Fig. 1a, exchange energy with each other faster than the temporal period. The qubit frequency spacing $\frac{\omega_q}{2\pi}$ can be tuned between 0 Hz and 5.5 kHz. We have mostly restricted ourselves to the first Brillouin zone, where both the quantum Rabi and the periodic quantum Rabi models coincide, see Methods, but also discuss the transition region. In the extreme coupling regime of $g \gg \omega$ that we study, striking dynamics is observed at this point.

To begin with, we have monitored the atomic dynamics in position space by spatial imaging of the atomic cloud following its manipulation in the combined lattice and harmonic dipole trapping potential, as well as the atomic dynamics in momentum space by time-of-flight imaging. Using both measurements, the expectation value for the bosonic excitation number $\langle N \rangle = \frac{m\omega}{2\hbar} (\langle x^2 \rangle + \frac{1}{m^2\omega^2} \langle q^2 \rangle)$ can be determined. For these measurements, atoms are initially prepared at a momentum centered at $|-2\hbar k\rangle$, corresponding to a quasimomentum of $q = 0$ in the Brillouin zone, see Fig. 1d, and $\langle N \rangle = 0$. The blue dots in Fig. 2a show the observed temporal dynamics of the atomic excitation number in our system for a qubit splitting $\frac{\omega_q}{2\pi} = 586(6)$ Hz, which is of the order of

the harmonic trapping frequency $\frac{\omega}{2\pi} = 346(7)$ Hz. The observed increase of the excitation number $\langle N \rangle$ with time shows that the deep strong coupling regime is reached. The experimental data is in good agreement with theory based on numerically integrating the Schrödinger equation using the Hamiltonian of eq. 1, for the extremely large coupling strength of $\frac{g}{\omega} \cong 6.5$ used in the experiment (blue line). For comparison, the orange data points correspond to data for the larger qubit spacing of $\frac{\omega_q}{2\pi} = 5200(50)$ Hz, at which the dispersive deep strong coupling regime is reached, for which the increase in excitation number occurs more slowly. Next, we have recorded experimental data for different ratios of the relative coupling strength $\frac{g}{\omega}$. For this, the trapping frequency ω was tuned, and Fig. 2b gives corresponding data recorded at the fixed interaction time of $t = \frac{3\pi}{8\omega}$ versus the relative coupling strength $\frac{g}{\omega}$ both for a qubit frequency of $\frac{\omega_q}{2\pi} = 590(6)$ Hz (blue dots) and $\frac{\omega_q}{2\pi} = 5850(60)$ Hz (orange triangles) respectively. The data shows that the excitation number increases with the relative coupling strength $\frac{g}{\omega}$, and the achieved large values of up to above 70 excitation quanta, which are achieved at the used short subcycle interaction time, i.e. being much shorter than the period $\frac{2\pi}{\omega}$, gives evidence that we operate in the regime of the coupling strength g far exceeding the oscillator frequency ω . This can be seen analytically when for sake of simplicity as a lower bound the formula for the stationary value of the excitation number in the slow qubit approximation $\omega_q \cong 0$ of $\frac{g}{\omega} \geq \frac{\sqrt{\langle N \rangle}}{2}$ is used (see Methods). For a quantitative comparison, see the good agreement of the experimental data with theory in the two different regimes.

Next, we have analyzed the variation of the mean displacement $\langle x \rangle$ of the atomic cloud from the trap center versus time. For this measurement, atoms are prepared at momentum of $|-2\hbar k\rangle$ and after evolution in the combined lattice and harmonic trapping potential imaged in real space. Corresponding experimental data is shown in Fig. 3a as a function of interaction time for different values of the qubit frequency ω_q , as tuned by adjusting the lattice depth. For a vanishing depth of the lattice potential $\omega_q \rightarrow 0$, we observe the onset of a harmonic oscillation in the harmonic trapping

potential, while for increasing lattice depth, i.e., a non-vanishing value of the qubit spacing ω_q , the observed displacement is reduced, and the evolution for stronger lattice potentials becomes nonharmonic. From the observed displacement of the $\omega_q = 0$ data, we can readily determine the ratio of the coupling to the oscillation frequency, which equals $\frac{g}{\omega} = \frac{x_{m,0}}{x_{ho}}$, where $x_{m,0} = \frac{2\hbar k}{m\omega}$ is the amplitude of the classical oscillation in the absence of a lattice potential and $x_{ho} = \sqrt{\frac{2\hbar}{m\omega}} \approx 0.82 \mu\text{m}$ the size of the harmonic oscillator ground state wavepacket. From this, we obtain $\frac{g}{\omega} = 5.6(6)$, which is near the above-described result for the coupling ratio. To put the deep strong coupling condition $\frac{g}{\omega} \gg 1$ differently, only in this limit the splitting of wavepackets in the bosonic mode expected for the nontrivial case of a nonvanishing qubit splitting can exceed the wavepacket size. That is, only in the deep strong coupling regime we can expect to observe distinguishable dynamics not only in the qubit occupation, but also in the bosonic field modes. The time evolution of the observed mean displacement $\langle x \rangle$ of the data with nonvanishing qubit spacing depicted in Fig. 3a agrees with simulations of the quantum Rabi model in the deep strong coupling regime, depicted as lines. A more detailed analysis of real space data in our system is limited by the finite instrumental resolution of our imaging system.

We have in more detail analyzed the momentum space data obtained by the far-field time of flight imaging, from which both the quasimomentum q and the band index n_b of Bloch bands, with $n_b = 0$ and 1 for momenta measured in the absence of a trapping potential of $p = -2\hbar k + q$ and $p = +2\hbar k + q$ respectively, can be derived (see Methods). Figures 3b and 3c show both the variation of the mean atomic quasimomentum $\langle q \rangle$ and the mean Bloch band occupation $\langle \sigma_x \rangle$, which in the basis of the band eigenstates can be written as $\hat{\sigma}_x = |n_b = 0\rangle\langle n_b = 0| - |n_b = 1\rangle\langle n_b = 1|$, with time along with theory. Remarkably, at small lattice depth, corresponding to a low value of ω_q , we observe a temporally nearly constant value of the Bloch band occupation $\langle \sigma_x \rangle$. This is understood as signal preparation, detection and the system Hamiltonian – the latter in the unusual regime of $g \gg \omega$ being dominated by the interaction term – all are diagonal in the same basis, the eigenbasis of the

Pauli matrix σ_x . In contrast, for larger lattice depth, i.e., with increased ω_q , Rabi-oscillations between the co- and counterpropagating atomic wavepackets are observed. This is most clearly visible for the data shown by the red squares for $\frac{\omega_q}{2\pi} \cong 3600(40)$ Hz, which is far above the frequency of the bosonic mode $\frac{\omega}{2\pi} \cong 346(7)$ Hz, and of the order of the coupling constant $\frac{g}{2\pi} \cong 2275(50)$ Hz. The experimental data are shown in Fig. 3c, which for different values of the qubit splitting well agrees with theory expectations, clearly shows that we work far in the deep strong coupling regime, with $g \gg \omega$.

One also finds that near the largest investigated interaction times the experimental data (data points) visible in Figs. 3b and 3c starts to deviate from the theory curves (lines), which were derived based on the quantum Rabi model, as understood from that the edge of the Brillouin zone at $t = \frac{\pi}{2\omega}$ is reached, upon which it becomes relevant that our system realizes a periodic variant of the quantum Rabi model. This is most clearly seen for the data sets recorded with the smallest qubit spacings. Theory predictions based on the periodic quantum Rabi model, which qualitatively reproduce the experimental data also near the band edge, are shown by semi-translucent lines.

In further measurements, we have prepared atoms in the qubit ground state $|g\rangle$ and excited state $|e\rangle$ respectively formed by the Bloch bands and studied the temporal variation of the qubit population. As described above, the qubit states correspond to coherent superpositions of the momentum picture states $|\pm 2\hbar k\rangle$ respectively, and to prepare these states Bragg transitions were driven with counterpropagating momentum transfer using the Raman beams with the corresponding phase difference imprinted. We again start at a vanishing bosonic mode quantum number ($\langle N \rangle = 0$), so the initial states $|g, 0\rangle$, $|e, 0\rangle$ prepared in this way have different parity¹². For detection, given that the qubit occupation is encoded in the relative phase of two wavepackets, at the end of the measurement atoms were first adiabatically moved away from the bandgap by chirping the four-photon lattice potential, which remaps the upper and lower bands $|e\rangle$ and $|g\rangle$ to the bare states

$|2\hbar k\rangle$ and $| - 2\hbar k\rangle$ respectively, and then observing the band population. Experimental results for the variation of the measured qubit population difference $\langle\sigma_z\rangle = \langle(|e\rangle\langle e| - |g\rangle\langle g|)\rangle$ with time are shown in Fig. 4a. Here the blue dots and yellow triangles correspond to an initial population in the ground state for a qubit frequency ω_q of $\omega_q \rightarrow 0$ and 1050(10) Hz respectively, and the red squares and green triangles to preparation in the excited state for the corresponding qubit frequencies. In all cases, rapid decay of the population difference $\langle\sigma_z\rangle$ with time is observed, in agreement with theoretical predictions, as understood from strong interactions of the qubit states with the bosonic field mode for the highly entangled nature of the system ground state¹². We attribute the visible deviation from theory for the largest investigated interaction times of near 700 μ s, at which the end of the Brillouin zone is reached, to non-adiabatic transitions occurring in the used experimental band-mapping readout scheme.

We have also determined the variation of the mean excitation number $\langle N \rangle$ on the interaction time, as shown in Fig. 4b for both atoms initially in the qubit ground state $|g\rangle$ (blue dots) and the excited state $|e\rangle$ (orange triangles) respectively. Here an enhancement of the excitation number for atoms initially in the upper qubit state with respect to that when preparing in the lower state is observed. The difference is smaller than theoretical predictions, and we attribute the reduced contrast to the imperfect resolution of our imaging system, which reduces the distinguishability of the diffraction peaks. Figure 4c shows the variation of the difference of the excitation number $\langle N \rangle$ between when preparing the qubit in the ground and excited states respectively on both time and qubit frequency ω_q . This generalizes the results shown in Fig. 4b to different qubit frequency spacings. While for small spacings the sensitivity of the excitation number on the initial state of the qubit is small, at qubit frequencies above $\frac{\omega_q}{2\pi} \approx 1$ kHz a clear difference is visible. While for the simple case of $\omega_q = 0$ the atomic wavepacket superposition oscillating in the trapping potential can be expressed by the Schrödinger cat states $\frac{1}{\sqrt{2}}\left(\left|\frac{ig}{\omega}\right\rangle \pm \left|-\frac{ig}{\omega}\right\rangle\right)$ respectively, for a nonvanishing qubit frequency ω_q the quantum states become much more complex entangled states. The experimental findings of Fig. 4c

demonstrate the phase-dependent behavior of the quantum Rabi dynamics in the deep strong coupling regime. The observations agree with the theory, see the corresponding plot in Fig. 4d for comparison.

Our experiment demonstrates that an atom-based approach can realize quantum Rabi physics at previously unobtainable high values of the coupling strength. A regime where the coupling strength dominates over all other energy scales in the system Hamiltonian has been reached, and the characteristic dynamics was mapped out.

For the future, extensions of this work can include quantum information processing based on qubits encoded in the vibrational dynamics of cold atoms in engineered superpositions of periodic lattices and slowly varying dipole trapping potentials. For coupling of qubits, digital techniques, alternating between tightly confined interaction and qubit manipulation periods following here demonstrated techniques can be envisioned ²². It also will be interesting to extend the present work to longer interaction times, as to study predictions of the periodic quantum Rabi model and observe collapse and revival patterns of the initial state ¹⁹. Other interesting future work includes the search for novel phase transitions of the spin-boson model ^{23,24}.

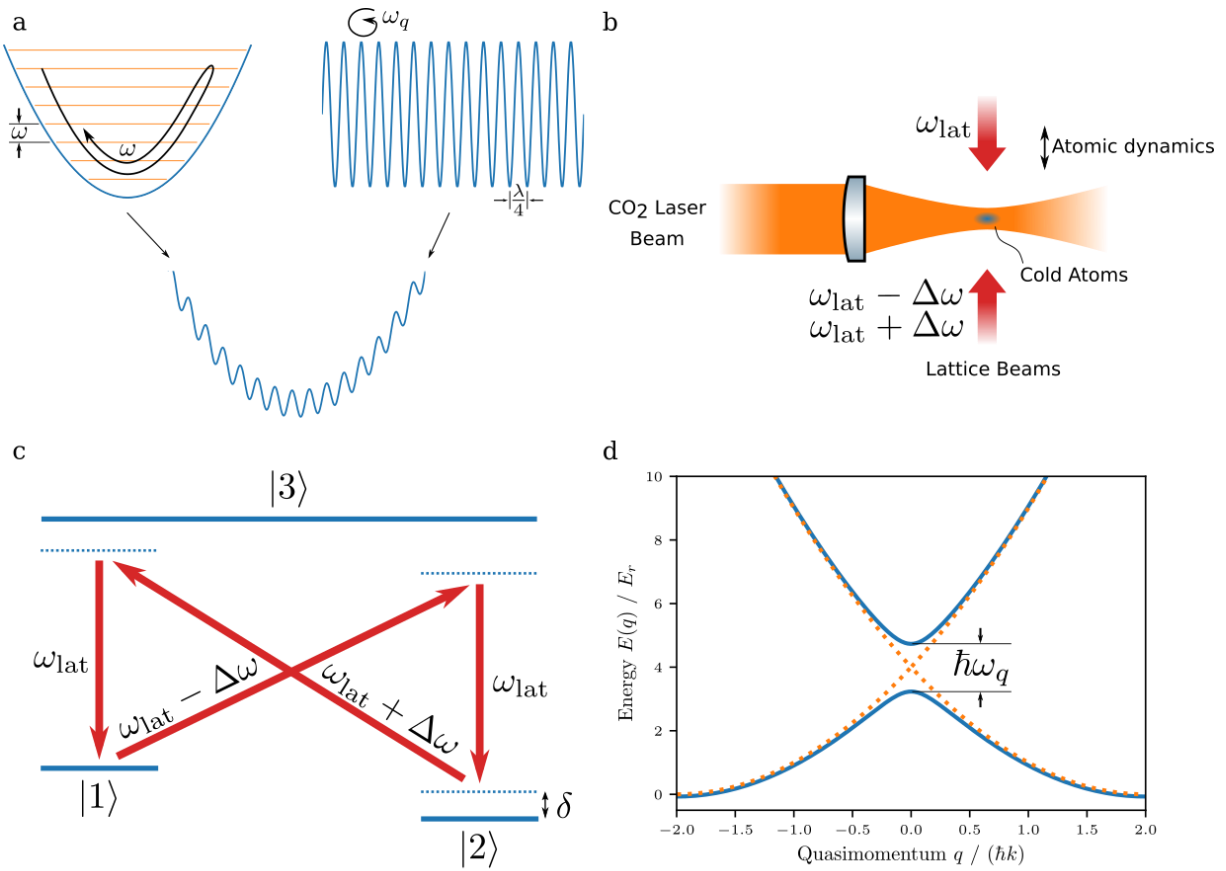


Fig. 1: Experimental schematic. **a**, Atoms are exposed to the combined potential obtained by superimposing a harmonic trapping potential (left) generated by a focused CO₂-laser beam and a lattice potential of spatial periodicity $\frac{\lambda}{4}$ (right). The relevant oscillatory modes, of frequency ω for the oscillation in the harmonic trapping potential and ω_q for oscillation at the first band gap of the lattice, are indicated. For atoms moving in the combined potential, the two modes are extremely strongly coupled. **b**, Schematic of the experimental setup along with the optical frequency components in the optical lattice beams used to synthesize the four-photon lattice potential of periodicity $\frac{\lambda}{4}$, see **c** for the coupling scheme. **d**, Dispersion relation of rubidium atoms in the lattice (blue) versus the atomic quasimomentum along with the dispersion of free atoms in states $|2\hbar k + q\rangle$ and $| - 2\hbar k + q\rangle$ (orange dotted). At the position of the crossing, atoms in the lower and upper band correspond to states $|g\rangle$ and $|e\rangle$ respectively of the two-level qubit system.

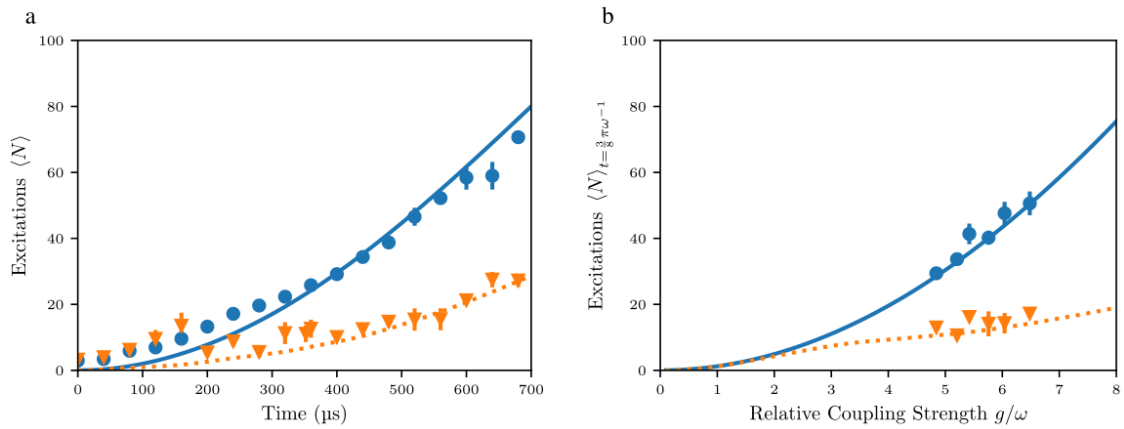


Figure 2: Creating system excitations. **a**, Variation of the number of excitation quanta $\langle N \rangle$ in the potential versus interaction time for a relative coupling strength $\frac{g}{\omega} = 6.58(7)$ i.e., far in the deep strong coupling regime, and qubit spacings of $\frac{\omega_q}{2\pi} = 586(6)$ Hz (blue dots) and $5200(50)$ Hz (orange triangles). The lines are theory. Atoms for this measurement are prepared in the momentum state $| -2\hbar k \rangle$ in the center of the harmonic trapping potential. **b**, Variation of the number of excitations on the relative coupling strength $\frac{g}{\omega}$. Here a fixed interaction time of $\frac{3}{8}\pi\omega^{-1}$ was used, and blue dots and orange triangles correspond to qubit spacings $\frac{\omega_q}{2\pi} = 590(6)$ Hz and $5850(60)$ Hz respectively.

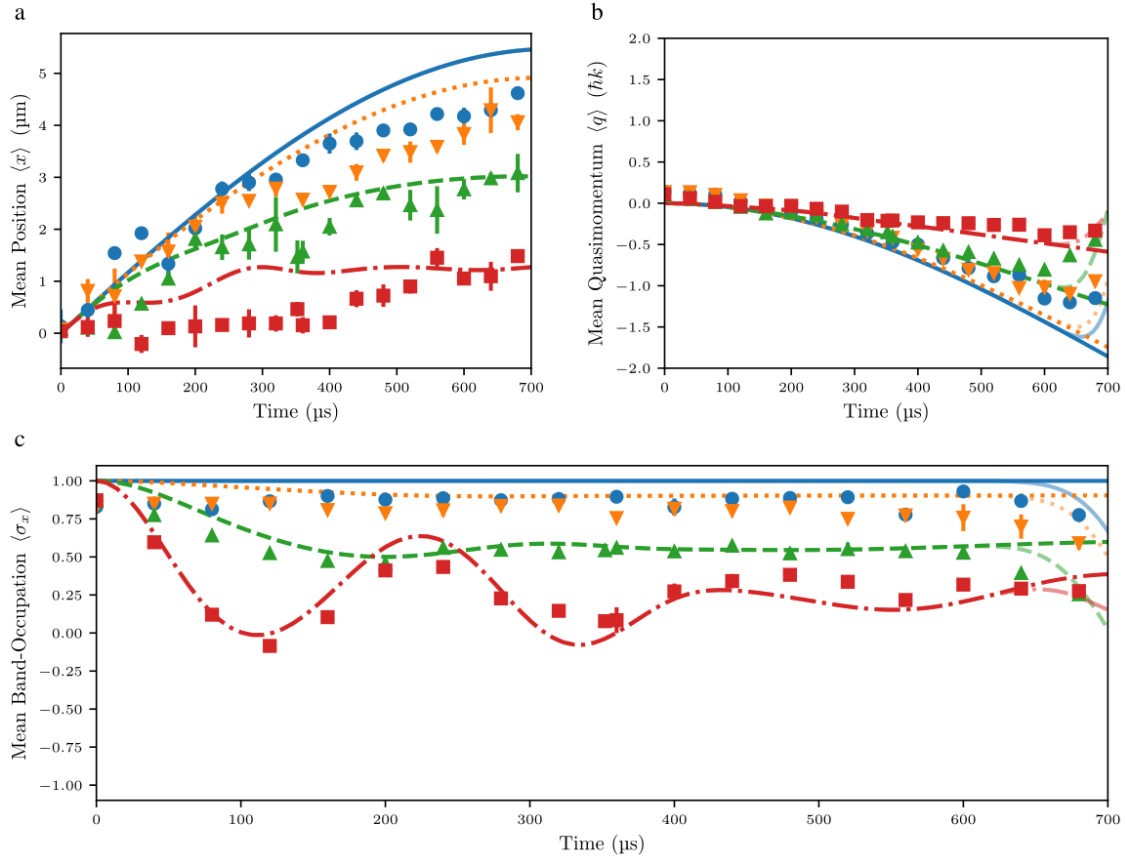


Fig. 3: Revealing the time evolution of system parameters. **a**, Variation of the mean value of the atomic cloud position $\langle x \rangle$ on the interaction time. The used relative coupling strength is $\frac{g}{\omega} = 6.58(7)$ and the used qubit spacings $\frac{\omega_q}{2\pi}$ were 0 Hz (blue dots), 586(6) Hz (orange triangles), 1660(20) Hz (green upside-down triangles), and 3600(40) Hz (red squares) respectively. The system is initially prepared in the momentum state $| -2\hbar k \rangle$. Theory results for the quantum Rabi and the periodic quantum Rabi models are represented by non-transparent and semi-transparent lines, respectively. **b**, Time evolution of the observed mean atomic quasimomentum $\langle q \rangle$ and **c**, the Bloch band occupation $\langle \sigma_x \rangle$ for corresponding values of the qubit spacing.

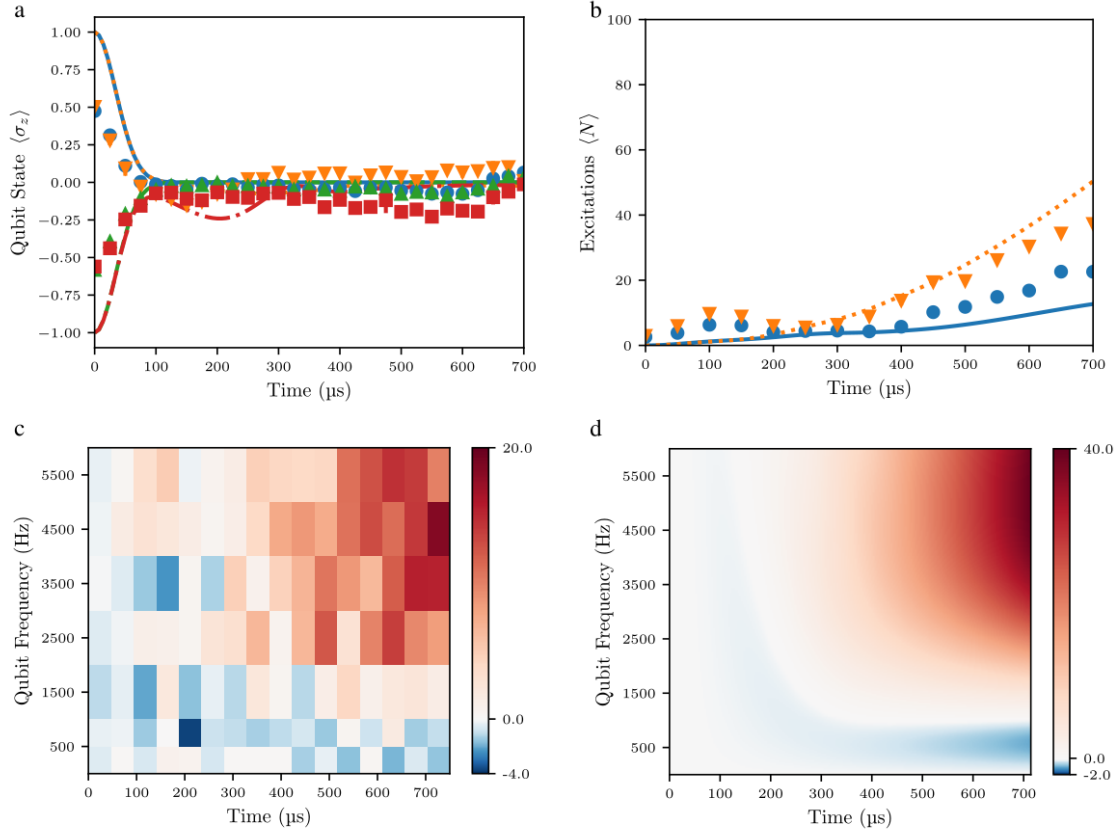


Fig. 4: Preparing atoms in qubit states. **a**, Time evolution of the qubit excitation $\langle \sigma_z \rangle$ following preparation of atoms in lower (orange triangles) and upper (red squares) states of the two-state system for a qubit spacing $\frac{\omega_q}{2\pi} = 1050(10)$ Hz. For comparison, the blue dots and green upside-down triangles correspond to measurements with $\omega_q = 0$. The lines are theory. $\frac{g}{\omega} = 6.5(5)$ in all measurements. **b**, Variation of the mean excitation number $\langle N \rangle$ on the interaction time for atoms initially prepared in the ground (blue dots) and the excited qubit states (orange triangles) respectively for $\frac{\omega_q}{2\pi} = 4660(50)$ Hz, along with theory (lines). **c**, Experimental data for the difference in the mean excitation number $\langle N \rangle_{|e\rangle} - \langle N \rangle_{|g\rangle}$ observed when preparing atoms initially in qubit excited and ground states respectively on both interaction time and qubit spacing represented in color code. **d**, Corresponding theory expectations.

Acknowledgements

We acknowledge support by the DFG within the focused research center SFB/TR 185 (277625399) and the Cluster of Excellence ML4Q (EXC 2004/1 – 390534769), the QMiCS (820505) and OpenSuperQ (820363) projects of the EU Flagship on Quantum Technologies, the National Natural Science Foundation of China (NSFC) (12075145), the Shanghai Government grant STCSM (2019SHZDZX01-ZX04), the Spanish Government PGC2018-095113-B-I00 (MCIU/AEI/FEDER, UE), the Basque Government IT986-16, and the FET Open Quromorphic and EPIQUS EU projects.

Methods

Experimental setup and procedure

Our experimental apparatus, see also the schematics shown in Fig. 1b of the main text, is a modified version of a setup used in earlier works²⁵. Inside a vacuum apparatus, cold rubidium atoms (⁸⁷Rb) collected in a magneto-optic trap are loaded into the dipole trapping potential induced by a beam focused to 42 μm diameter derived from a CO₂-laser operating near 10.6 μm wavelength. The atoms are evaporatively cooled to quantum degeneracy by lowering the depth of the dipole potential. In the final stages of the cooling, a magnetic quadrupole field is activated, which allows to generate a spin-polarized Bose-Einstein condensate in the $m_F = 1$ component of the $F = 1$ hyperfine ground state. To keep interaction effects small, here we work with small condensate numbers of typically 2500 atoms, as achieved by ramping the depth of the trapping potential in evaporative cooling to lower values than needed to achieve condensation to reduce the number of confined atoms. Subsequently, the dipole trapping potential is ramped up adiabatically within 250 ms to reach the desired values of the trapping frequency ω , see also the main text, for simulation of the quantum Rabi model. Typical beam powers are 32 W, 30 mW, and 100 mW during loading, the final stage of evaporative cooling, and quantum Rabi manipulation phases, respectively. In the latter phase, atoms remain well confined in the center of the Gaussian beam, in a range where the dipole trapping potential can well be described as a harmonic potential. The estimated decoherence time from photon scattering from the mid-infrared trapping laser beam in the quantum Rabi manipulation phase is 1.7×10^{-5} /s, i.e., is negligible. In practice, decoherence will be determined by scattering from the Raman beams and atomic interaction effects.

The method used to generate a high spatial harmonic lattice potential of periodicity $\frac{\lambda}{4}$, where $\lambda \simeq 783.5$ nm (which is detuned 3.5 nm from the rubidium D2-line) denotes the wavelength of the driving laser beams, relies on four-photon Raman processes²⁰. The transitions are driven in a three-level configuration with two stable ground states $|1\rangle$ and $|2\rangle$ and one spontaneously decaying

excited state $|3\rangle$ by a beam of frequency ω_l and two counterpropagating superimposed beams of frequencies $\omega_{\text{lat}} + \Delta\omega_{\text{lat}}$ and $\omega_{\text{lat}} - \Delta\omega_{\text{lat}}$. The $m_F = -1$ and $m_F = 0$ components of $5S_{1/2}, F = 1$ constitute the used ground states and the $5P_{3/2}$ manifold serves as the excited state of the three-level configuration. Atomic momentum is exchanged with the driving light field in units of four-photon momenta, which is a factor two above that of the relevant processes in a usual standing wave lattice induced by two-photon processes. Correspondingly, the spatial periodicity of the induced potential is a factor two smaller and equals $\frac{\lambda}{4}$.²⁰ In the experiment, we typically use a magnetic bias field of 1 G to remove the degeneracy of Zeeman sublevels and a frequency difference $\frac{\Delta\omega_Z}{2\pi} \simeq 1.6$ MHz.

In the experimental sequence, following the ramping up of the CO₂-laser beam intensity to the desired harmonic trapping frequency, atoms are prepared near the first avoided crossing of the lattice band structure (Fig. 1d) by means of Bragg diffraction. For the used lattice with spatial periodicity $\frac{\lambda}{4}$ usual Bragg diffraction, transferring momentum in units of two-photon momenta, can be used to prepare atoms at the position of the first band crossing. For the experimental data shown in Fig. 4, with qubit states $|g\rangle$ and $|e\rangle$ respectively as the initial states, two simultaneously performed Bragg pulses with opposite directions of the momentum transfer were used with the relative phase of the pulses allowing to set the desired qubit initial state. Following preparation, atoms were left in the desired combined potential of lattice and harmonic trapping for quantum Rabi manipulation for a variable interaction time.

Subsequent detection of the atomic cloud was performed after extinguishing both the lattice and the dipole trapping beams. For this, absorption imaging of the atomic sample was employed onto a sCMOS camera. During the experiments described in the main text, both measurements probing the real-space distribution are carried out by probing directly following the experiment, as well as far-field time-of-flight imaging probing the momentum distribution were performed. For an analysis of measurements of the rms displacement $\langle x^2 \rangle$ of the atomic cloud from the trap center, the

experimental image data was first deconvoluted by the point spread function of the imaging system (of near 6.5 μm instrumental resolution) determined in an independent measurement before analysis of this moment from a series of measurement. Example images after deconvolution are shown in Fig. M1a.

The momentum p measured in the absence of a trapping potential maps onto the quasimomentum q and the band index $n_b \in \{0,1\} \rightarrow \{-2\hbar k, 2\hbar k\}$ mapping the basis states of our qubit state via $p = q + 2\hbar k(2n_b - 1)$. Example time of flight images to obtain the momentum p and subsequently quasimomentum q and band index n_b are shown in Fig. M1b.

Theoretical methods

The single-particle Hamiltonian for a cloud of ultracold atoms is described by the sum of a harmonic part, which includes the kinetic energy of the atoms and the harmonic trap, and a periodic potential,

$$\hat{H} = \frac{\hat{p}^2}{2m} + \frac{m\omega^2}{2}\hat{x}^2 + \frac{V}{2}\cos(4k\hat{x}), \quad (M1)$$

where $\hat{p} = -i\hbar\frac{d}{dx}$ and \hat{x} are momentum and position of an atom of mass m , respectively. If we write this Hamiltonian in the Bloch basis function $\langle x|\phi_n(q)\rangle = e^{iqx/\hbar}e^{-i2kx}e^{i4nkx}$ and we project to the two lowest energy bands, it is recast into

$$\hat{H} = \frac{\hat{q}^2}{2m} + \frac{m\omega^2}{2}\hat{x}^2 + \frac{2\hbar k}{m}\begin{pmatrix} 1 & 0 \\ 0 & -1 \end{pmatrix}\hat{q} + \frac{V}{4}\begin{pmatrix} 0 & 1 \\ 1 & 0 \end{pmatrix}. \quad (M2)$$

Defining creation and annihilation operators $\hat{a} = \sqrt{\frac{m\omega}{2\hbar}}(\hat{x} + \frac{i}{m\omega}\hat{q})$ and $\hat{a}^\dagger = \sqrt{\frac{m\omega}{2\hbar}}(\hat{x} - \frac{i}{m\omega}\hat{q})$, while rotating the qubit (band index) with the unitary operator $U = \frac{1}{\sqrt{2}}\begin{pmatrix} 1 & 1 \\ 1 & -1 \end{pmatrix}$, and defining the Pauli matrices in the rotated basis as

$$\sigma_x = |n=0\rangle\langle n=0| - |n=1\rangle\langle n=1|$$

$$\sigma_z = |n=1\rangle\langle n=0| + |n=0\rangle\langle n=1|$$

the total system Hamiltonian is the one given in Eq. (1).

In what follows, we would like to understand the occupation number, or number of photons, in a quenched experiment starting with the ground state of a cavity mode with frequency ω in a Rabi model, where the frequency of the qubit is set to zero, i.e. $\omega_q = 0$, and the coupling strength of the cavity and qubit is given by g ,

$$\begin{aligned} H_{\omega_q=0} &= \omega \left(N + \frac{1}{2} \right) + g\sigma_x(a + a^\dagger) \\ &= \omega \left(a^\dagger + \frac{g\sigma_x}{\omega} \right) \left(a + \frac{g\sigma_x}{\omega} \right) + \frac{\omega}{2} - \frac{g^2}{\omega} \end{aligned} \quad (M3)$$

As it can be directly seen from the second line, this Hamiltonian is diagonal with the displaced cavity operators

$$b = a + \frac{g\sigma_x}{\omega} = a + \alpha,$$

where the displacement operator is given by

$$D(\alpha) = e^{\alpha a^\dagger - \alpha^* a} = e^{-\frac{|\alpha|^2}{2}} e^{\alpha a^\dagger} e^{-\alpha^* a},$$

for a general α parameter.

The action of the time evolution of a displaced Hamiltonian for a cavity mode on the vacuum, i.e., no excitations, is given by

$$\begin{aligned} e^{iH(\alpha)t} |0\rangle &= D(-\alpha) e^{iH(0)t} D(\alpha) |0\rangle = e^{\frac{i\omega t}{2}} e^{\frac{ig^2 t}{\omega}} D(-\alpha) |e^{-i\omega t} \alpha\rangle \\ &= e^{\frac{i\omega t}{2}} e^{\frac{ig^2 t}{\omega}} e^{\text{Im}(|\alpha|^2 e^{i\omega t})} D[\alpha(e^{-i\omega t} - 1)] |0\rangle. \end{aligned}$$

From this expression, we can derive the expectation value in the number of excitations for an interaction time t

$$\langle N \rangle = |\alpha(t)|^2 = 4|\alpha|^2 \sin^2\left(\frac{\omega t}{2}\right). \quad (M4)$$

Correspondingly, with $\alpha = \frac{g}{\omega}$, the maximum number of the expectation value $\langle N \rangle$ is given by

$$N_{\max} = 4|\alpha|^2 = \frac{4g^2}{\omega^2}. \quad (M5)$$

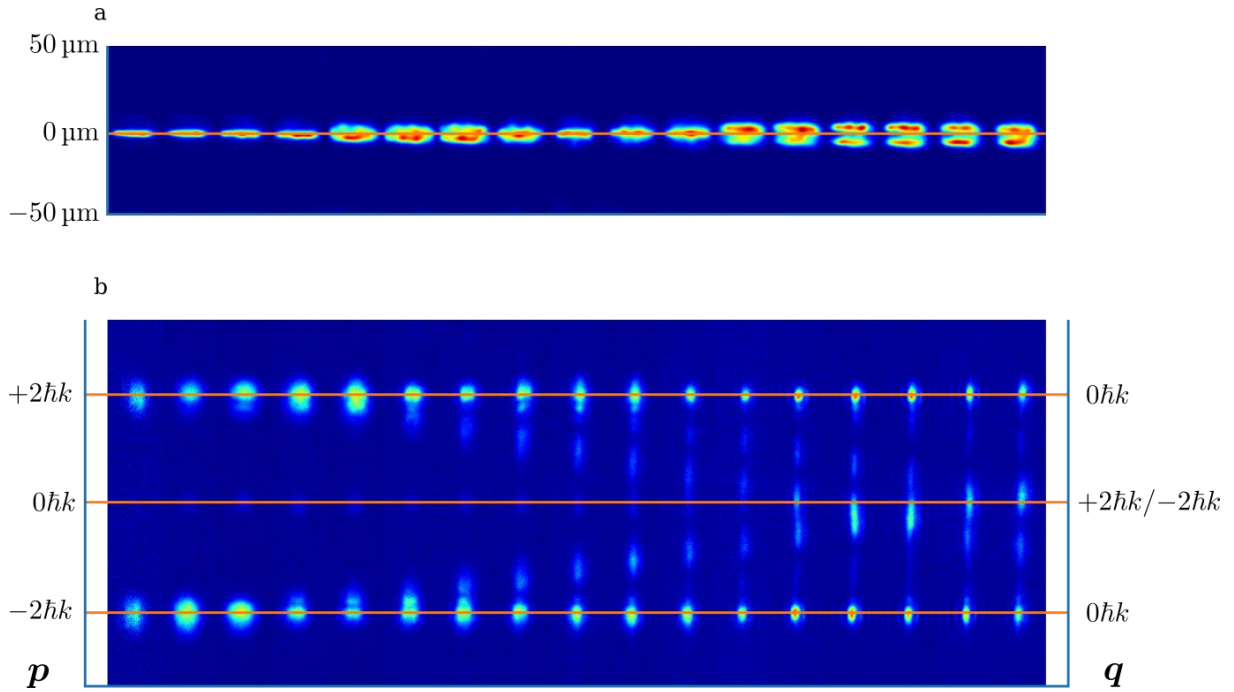


Fig. M1: Examples of obtained image data. **a**, Real space images of the system initially prepared in the qubit excited state, with $\frac{\omega_q}{2\pi} = 2380(40)$ Hz and $\frac{g}{\omega} = 6.5(5)$, after deconvolution of the obtained images. From left to right the interaction time increases in steps of 50 μ s. Despite the limited optical resolution, the separation of the atomic clouds is observed. **b**, Time of flight images of the same state as shown in subfigure a. The numbers on the left-hand side represent the measured real momentum p of the atomic clouds, while the right-hand side shows the obtained quasimomentum q .

References

1. Rabi, I. I., On the process of space quantization. *Phys. Rev.* **49**, 324 (1936).
2. Braak, D., Chen, Q.-H., Batchelor, M. T. & Solano, E., Semi-classical and quantum Rabi models: in celebration of 80 years. *J. Phys. A* **49**, 300301 (2016).
3. Nataf, P. & Ciuti, C., Protected quantum computation with multiple resonators in ultrastrong coupling circuit QED. *Phys. Rev. Lett.* **107**, 190402 (2011).
4. Romero, G., Ballester, D., Wang, Y., Scarani, V. & Solano, E., Ultrafast quantum gates in circuit QED. *Phys. Rev. Lett.* **108**, 120501 (2012).
5. Kyaw, T. H., Herrera-Marti, D. A., Solano, E., Romero, G. & Kwek, L.-C., Creation of quantum error correcting codes in the ultrastrong coupling regime. *Phys. Rev. B* **91**, 064503 (2015).
6. Rossatto, D. Z. *et al.*, Entangling polaritons via dynamical Casimir effect in circuit quantum electrodynamics. *Phys. Rev. B* **93**, 094514 (2016).
7. Forn-Díaz, P., Lamata, L., Rico, E., Kono, J. & Solano, E., Ultrastrong coupling regimes of light-matter interaction. *Rev. Mod. Phys.* **91**, 025005 (2019).
8. Langford, N. *et al.*, Experimentally simulating the dynamics of quantum light and matter at deep-strong coupling. *Nat. Commun.* **8**, 1715 (2017).
9. Marković, D. *et al.*, Demonstration of an effective ultrastrong coupling between two oscillators. *Phys. Rev. Lett.* **121**, 040505 (2018).
10. Haroche, S. & Raimond, J.-M., in *Strong Light-matter Coupling: From Atoms To Solid-state Systems*, edited by Auffèves, A. *et al.* (World Scientific, 2013), pp. 1-36.
11. Ciuti, C., Bastard, G. & Carusotto, I., Quantum vacuum properties of the intersubband cavity polariton field. *Phys. Rev. B* **72**, 115303 (2005).

12. Casanova, J., Romero, G., Lizuain, I., García Ripoll, J. J. & Solano, E., Deep strong coupling regime of the Jaynes-Cummings model. *Phys. Rev. Lett.* **105**, 263603 (2010).
13. Dareau, A., Meng, Y., Schneeweiss, P. & Rauschenbeutel, A., Observation of ultrastrong spin-motion coupling for cold atoms in optical microtraps. *Phys. Rev. Lett.* **121**, 253603 (2018).
14. Lv, D. *et al.*, Quantum simulation of the quantum Rabi model in a trapped ion. *Phys. Rev. X* **8**, 021027 (2018).
15. Yoshihara, F. *et al.*, Superconducting qubit--oscillator circuit beyond the ultrastrong-coupling regime. *Nat. Phys.* **13**, 44-47 (2017).
16. Peropadre, B., Forn-Díaz, P., Solano, E. & García-Ripoll, J. J., Switchable ultrastrong coupling in circuit QED. *Phys. Rev. Lett.* **105**, 023601 (2010).
17. Jaynes, E. T. & Cummings, F. W., Comparison of quantum and semiclassical radiation theories with application to the beam maser. *Proc. IEEE* **51**, 89--109 (1963).
18. Braak, D., Integrability of the Rabi model. *Phys. Rev. Lett.* **107**, 100401 (2011).
19. Felicetti, S. *et al.*, Quantum Rabi model in the Brillouin zone with ultracold atoms. *Phys. Rev. A* **95**, 013827 (2017).
20. Ritt, G., Geckeler, C., Salger, T., Cennini, G. & Weitz, M., Fourier synthesis of optical potentials for atomic quantum gase. *Phys. Rev. A* **74**, 063622 (2006).
21. Salger, T., Geckeler, C., Kling, S. & Weitz, M., Atomic Landau-Zener tunneling in Fourier-synthesized optical lattices. *Phys. Rev. Lett.* **99**, 190405 (2007).
22. Lamata, L., Parra-Rodriguez, A., Sanz, M. & Solano, E., Digital-analog quantum simulations with superconducting circuits. *Adv. Phys.: X* **3**, 1457981 (2018).

23. Hwang, M.-J., Puebla, R. & Plenio, M. B., Quantum phase transition and universal dynamics in the Rabi model. *Phys. Rev. Lett.* **115**, 180404 (2015).
24. Heyl, M., Dynamical quantum phase transitions: a review. *Rep. Prog. Phys.* **81**, 054001 (2018).
25. Cennini, G., Ritt, G., Geckeler, C. & Weitz, M., Bose-Einstein condensation in a CO₂-laser optical dipole trap. *Appl. Phys. B* **77**, 773-779 (2003).